RSC Advances

Reinforcement of nanostructured reduced graphene oxide: A facile approach to develop high-performance nanocomposite ultrafiltration membranes minimizing the trade-off between flux and selectivity

Journal:	*RSC Advances*
Manuscript ID:	RA-ART-03-2015-005171.R1
Article Type:	Paper
Date Submitted by the Author:	05-May-2015

Complete List of Authors:	Pal, Avishek; Bhabha Atomic Research Centre, Membrane Development Section, Chemical Engineering Group Kar, Soumitra; Bhabha Atomic Research Centre, Membrane Development Section, Chemical Engineering Group Debnath, A K; Bhabha Atomic Research Centre, Technical Physics Division Aswal, D; Bhabha Atomic Research Centre, Technical Physics Division Bindal, R.C.; Bhabha Atomic Research Centre, Membrane Development Section, Chemical Engineering Group Tewari, P.K.; Homi Bhabha National Institute,

Cite this: DOI: 10.1039/c0xx00000x

www.rsc.org/xxxxxx

ARTICLE TYPE

Reinforcement of nanostructured reduced graphene oxide: A facile approach to develop high-performance nanocomposite ultrafiltration membranes minimizing the trade-off between flux and selectivity

Avishek Pal,[a] Soumitra Kar,*[a] A. K. Debnath,[b] D. K. Aswal,[b] R. C. Bindal[a] and P. K. Tewari[c]

[a]Membrane Development Section, Chemical Engineering Group, Bhabha Atomic Research Centre, Trombay, Mumbai – 400085, India

[b] Technical Physics Division, Bhabha Atomic Research Centre, Trombay, Mumbai – 400085, India

[c] Homi Bhabha National Institute, Mumbai – 400094, India

*Corresponding author. Tel.: 91-22-25594713; Fax: 91-22-25505151; E-mail address: soubiswa@barc.gov.in, soumitra.1stmay@gmail.com (Soumitra Kar)

Received (in XXX, XXX) Xth XXXXXXXXX 20XX, Accepted Xth XXXXXXXXX 20XX
DOI: 10.1039/b000000x

The salient features of nanostructured carbonaceous material like graphene or graphene oxide have provided innovative alternatives for development of nanocomposite membranes with better selectivity without having a compromise in throughput, which as a result have got promising role to play in desalination and water purification. Here, nanostructured reduced graphene oxide (nRGO) is synthesized from graphite powder and characterized. Using non-solvent induced phase inversion technique, a series of nanocomposite ultrafiltration (UF) membranes are developed by *in situ* impregnation of the as synthesized nRGO in polysulfone (Ps) polymer matrix with variation of nRGO from 1 to 8 w/w%. The physicochemical features and transport properties offered by the membranes are evaluated. Structural characterization of the Ps-nRGO composite UF membranes are done by X-ray photoelectron spectroscopy and Fourier Transform Infra-red spectroscopy. The variation in porous morphology of the membranes, on impregnation of nRGO is evaluated by scanning electron microscopy. Variation in skin surface topography is analyzed by atomic force microscopy. The change in surface hydrophilicity is evaluated by contact angle studies. The thermal and mechanical properties of the membranes are assessed by thermogravimetric analysis and tensile strength measurements, respectively. The studies reveal that an optimum loading of nRGO (2 w/w%) in Ps matrix resulted membranes with elimination of trade-off between the flux and selectivity that exists with the conventional UF membranes. In addition, the optimum loading of nRGO resulted in membranes with improved thermal and mechanical stability. Thus, impregnation of nRGO delivers emerging potential to lead to the development of an ideal membrane with desirable attributes.

1. Introduction

Membranes and membrane based separation processes are extensively used for water treatment applications. Membranes, however, in general suffer from a serious drawback of inherent trade-off between flux and selectivity. The efforts to increase the flux of a membrane often lead to decline in selectivity and vice versa.

The introduction of nanostructured materials as modifier, however, has opened up newer and more innovative options for development of membranes with newer and improved properties. Four classes of nanoscale materials are usually being evaluated as functional materials for water purification: (a) metal-containing nanoparticles,[1-6] (b) zeolites,[7,8] (c) carbon nanotubes[9-14] and (d) dendrimers.[15-20] The said materials are important with respect to water purification applications because of having high surface area and many high-energy disordered/defect sites suitable for contaminants uptake. Moreover, the particles can be desirably functionalized for specific uptake of contaminants.

The properties of nanomaterials can be truly exploited in impregnating them on to the membrane surface rather than using as-grown nanomaterials. The use of nanomaterials without a host matrix may increase the risk of leaching out of nanomaterials into product water making the water unsafe for usage. A lot of work on the development and application of nanocomposite membranes for water purification and waste water treatment have been carried out recently.[21-26]

In present scenario, graphene, which consists of a 2D sheet of sp^2-bonded carbon atoms in a hexagonal honeycomb lattice,[27] is drawing the attention of membranologists since it can lead to an ultimately thin membrane (one-atom thick) that can be practically possible. Graphene possibly is going to assume a unique and outstanding place in membrane industry because it has got the potential to provide an ideal membrane with better properties like mechanical strength, chemical & thermal stability and significant flux with no compromise in selectivity.[28,29] Since the flux across a membrane scales inversely with that of thickness of membrane, graphene can possibly outweigh the performance of conventional pressure driven membranes (thousand times thicker than graphene). Furthermore, incorporation of graphene, as nanofiller, into polymer matrix can also aid in improving the membrane performance. Polymeric nanocomposites of graphene derivatives have been used in the preparation of different materials to be used for fuel cell membrane,[30,31] ultrafiltration,[32-34] nanofiltration,[35] pervaporation[36] and gas separation[37] applications.

In contrast to the earlier works on graphene oxide (GO) impregnated UF membranes,[38,39] the present work aims at evaluation of performance of nanocomposite UF membranes upon incorporation of nanostructured reduced graphene oxide (nRGO). The idea of preferring nRGO as beneficial reinforcement material is executed with an endeavor to provide the membrane surface a balance of hydrophilicity (due to the oxygen containing functionalities present over graphene network) and

hydrophobicity (due to the inherent nature of graphene). Also, it is expected that nRGO, in contrary to GO, would enable a delayed demixing during phase inversion process of membrane fabrication resulting in finer pores on the membrane surface (leading to better rejection attributes of the membrane), while having macro-voids beneath the asymmetric top layer (resulting in no compromise in flux). In addition, the thermal stability of nRGO is better compared to GO which could lead to a membrane with improved thermal characteristics. [40] It is important to note that the permeation of water in a hydrophobic, atomically smooth nano-confinement is enhanced compared to permeation through the similar sized pores available in the virgin membrane (membrane without GO/nRGO).[41] Furthermore, the hydrophilic nature of GO is reduced in having nRGO as a reinforcement material, which would essentially pose lesser drag on the water molecules while they are finding ways through the numerous nanochannels,[42] which in turn should lead to better and unhindered water permeation compared to GO based UF membranes.

With these scientific facts in background, the present work is focused on development of polysulfone-nanostructured reduced graphene oxide (Ps-nRGO) based nanocomposite UF membranes employing the in-house synthesized nRGO as reinforcing material, following phase inversion technique. The performance of the membranes was evaluated in terms of pure water permeability and solute rejection studies. The synthesized nRGO was characterized using various instrumental techniques like Raman spectroscopy, X-ray photoelectron spectroscopy (XPS) and X-ray diffraction (XRD) analysis. Structural characterization of the Ps-nRGO composite UF membranes was carried out by XPS and Fourier Transform Infra-red (FTIR) spectroscopy. Variation in skin surface topography was analyzed by atomic force microscopy (AFM). The change in surface hydrophilicity was evaluated by contact angle studies. The thermal and mechanical properties of the membranes were assessed by thermogravimetric (TGA) analysis and tensile strength measurements, respectively. An ideal membrane with optimum throughput, and rejection attributes along with improved thermal and mechanical properties were obtained at 2 w/w % reinforcement of nRGO.

2. Experimental

2.1 Materials

Polysulfone (Ps, Mw: 30 kDa) from Solvay Speciality Polymers (India), N-methyl-2-pyrrolidone (NMP) (purity of ≥ 99 %, Sigma-Aldrich) and Polyvinyl pyrrolidone (PVP, K-30; M_W: 40 kDa), procured from SRL (India) were used to prepare polysulfone base membrane. Synthetic graphite powder (particle size: <20 μm) (Aldrich) was used as a raw material to

manufacture reduced graphene oxide for modification of a Ps polymer based UF membrane. Concentrated sulphuric acid, sodium nitrate, potassium permanganate, 30% hydrogen peroxide of analytical grades and hydrazine hydrate (GR 99%) were purchased from different manufacturer and used for the oxidation-reduction process to convert graphite into graphene oxide and then reduced graphene oxide.

2.2 Preparation of nRGO from graphite via GO

2.2.1 Synthesis of graphene oxide (GO) from graphite

Conversion of graphite into graphitic/ graphene oxide (GO) through the process of oxidation, following the modified Hummer's method,[43,44] was accomplished by treating a mixture of graphite flakes (3.0 g, 1 weight equivalent) and $NaNO_3$ (1.5 g, 0.5 weight equivalent) with concentrated H_2SO_4 (69 ml), followed by cooling the mixture to 0°C using an ice bath. Then, oxidizing agent $KMnO_4$ (9.0 g, 3 weight equivalent) was slowly added to the suspension in portions to maintain the reaction temperature below 20°C. The reaction mixture was warmed to 35°C and stirred for 7 hours, resulting in a progressive formation of brownish-grey colored thickened mixture, with diminishing in effervescence. Further, addition of $KMnO_4$ (9.0 g, 3 weight equivalent) was done in one portion, and the reaction mixture was stirred for 12 hours at 35°C. After completion of the reaction the system was allowed to cool down to room temperature and then poured onto ice-water mixture (400 ml) with 30% H_2O_2 (3 ml) to reduce the residual permanganate and manganese dioxide to colorless soluble manganese sulfate. The brown colored suspension was then turned yellowish brown in colour. The mixture was then purified following the filtration steps, where, the filtrate was centrifuged (4000 rpm for 4 hours), and then the supernatant was decanted away. The remaining solid material was then washed in succession with 500 ml of water, 200 ml of 30% HCl, and 200 ml of ethanol. The solid GO, thus obtained after the purification process was vacuum-dried overnight at room temperature.

2.2.2 Synthesis of nRGO from exfoliated GO

Partial de-oxygenation of the GO was achieved by hydrazine-assisted de-epoxidation of GO.[45] For this purpose, the as synthesized dried GO (400 mg) was suspended in distilled water (400 ml) with vigorous stirring, yielding an inhomogeneous yellowish brown dispersion. Prior to the reduction process, the dispersion was undergone ultrasonic treatment for 1 hour. Reduction process was carried out with hydrazine hydrate (the weight ratio of hydrazine hydrate/GO = 1) at 100°C temperature for 24 hours with continuous stirring. During

completion of reduction, the yellowish brown colored dispersion of graphene oxide in water turned black and the reduced sheets aggregated and precipitated. The partially reduced GO i.e. nRGO was collected by sequentially following few steps like isolation via filtration, washing with distilled water for several times and then drying at 60ºC for 24 hours under vacuum to remove the residual solvent. The oxidation-reduction process for conversion of graphite in GO and then into nRGO is represented through the reaction scheme as shown in Scheme1.

2.3 Characterization of the synthesized GO & nRGO

The spontaneous Raman spectra of the as synthesized GO & nRGO were recorded using a STR-300 micro-Raman spectrometer (SEKI Technotron, Japan) at room temperature. The samples were excited at 532 nm (power ~20 mW at the sample spot, DPSS) using a 10X objective lens (Olympus). The scattered light was collected by the same objective lens and a fiber-coupled 300 mm spectrograph (Acton series SP 2300i, 1200 gr/mm) and detected by a thermo-electric cooled (-75°C) charge-coupled device (CCD).

In order to study the structural variation of the membrane surface XPS measurements were carried out. For XPS characterization of the nRGO as well as of the control and composite UF membrane surface, a DESA-150 electron analyzer (Staib Instruments, Germany) equipped with Mg-Kα X-ray source (1253.6 eV) was employed. The spectrometer binding energy scale was calibrated with Au-$4f_{7/2}$ photopeak at a binding energy of 83.95 eV. The spectrum was recorded as the intensity (number of counts per second) versus binding energy (BE). Curve fitting of the multiplex photopeaks was performed using Gaussion functions employing a least-squares peak analysis software (XPSPEAK 4.1) and then peak areas as well as full width at half maximum (FWHM) were also determined.

Textural features of the synthesized GO and nRGO were characterized by XRD analysis on a Philips X'Pert pro X-ray diffractometer. The XRD patterns with Cu Kα radiation (λ = 1.5418 Å) at 40 Kv and 30 mA were recorded in the range of 2θ = 10–70° at a scan speed of 0.5° min^{-1}. The average crystallite sizes for the nRGO was determined using Debye-Scherrer's equation ($t = K\lambda/B \cos\theta$, where t = average crystallite size in Å, K = Scherrer constant usually taken as 0.9 Å, λ = X-ray wavelength, θ is the Bragg angle, and B = integral breadth of a reflection located at 2θ).

2.4 Preparation of Ps-nRGO composite UF membranes

The nanoadditive, nRGO at different weight fractions (1, 2, 4 and 8 w/w% of Ps) was exfoliated in NMP solvent by ultrasonication for

30 minutes. Each of the NMP solutions comprising of dispersed nRGO at varying weight fractions was then mixed with 10 g of Ps polymer and 30 (w/w)% PVP, as pore forming additive to prepare polymer solutions of concentration 25 (w/v) %. After vigorous stirring for 24 hours, the dope solutions obtained, were kept overnight at room temperature without stirring until no air bubbles appear in the solution. Asymmetric flat sheet type Ps-nRGO composite ultrafiltration membranes with a very thin and dense skin layer were prepared by non-solvent induced phase inversion method. The as-prepared dope solutions were employed to cast membranes onto a nonwoven polyester fabric as a support layer with a nominal thickness of 100 μm, using a lab developed doctor's knife device. The membranes were then immediately immersed in a gelling bath containing distilled water at room temperature for immersion precipitation. After primary phase separation and formation stage, the resulting nRGO embedded Ps membranes were taken out of water bath and kept in another water bath for 24 hours to allow adequate removal of the solvent (NMP) and leachable additive (PVP) from the membrane matrix in water. The entire casting process was carried out in a controlled atmospheric condition by maintaining the temperature of the surrounding enclosed atmosphere between 21-24^{o}C with a relative humidity of 30–35%. The UF membranes made under similar atmospheric conditions, employing 1, 2, 4 and 8 w/w% of nRGO are named as Ps-nRGO UF-1, Ps-nRGO UF-2, Ps-nRGO UF-3 and Ps-nRGO UF-4, respectively.

2.5 Characterisation of the Ps-nRGO composite UF membranes

2.5.1 Spectral characterization of skin surface of membranes by FTIR

Vibrational spectra of the nRGO embedded UF membranes with Ps base matrices were acquired by FTIR technique. For spectral acquisition in the attenuated total reflectance (ATR) mode, Bruker make Vertex 70 spectrometer system equipped with an ATR unit (ZnSe crystal, 45^{o} angle of incidence and refractive index 2.4) was employed. The membranes skin surface was faced down onto the ATR crystal element and lighter pressure was applied using a MIRacle high pressure clamp with torque-limited press. The radiation penetration depth was 2 μm. All infrared spectra were recorded in absorbance mode over two different wave number regions i.e. 800-1550 cm^{-1} and 2750-3750 cm^{-1} at an ambient temperature. For evaluation, 200 scans were taken with a spectral resolution of 2 cm^{-1}.

2.5.2 Determination of hydrophilic characters of membrane skin surfaces

Static sessile drop contact angle measurement on the skin surfaces of the Ps-nRGO composite UF

membranes were performed at an ambient temperature with contact angle measuring instrument DSA 100 of KRUSS, Germany to evaluate the hydrophilic behavior of the membranes with respect to the probe liquid, de-ionized water. The sessile drop was slowly and steadily formed on the membrane surface by depositing 3 µl of the de-ionized water with a microsyringe for a residence time of 60 seconds. Eight measurements on different locations of each membrane surface were performed to get the contact angles at membrane-water-air interphase and then the average of left and right contact angles yielded to get the equilibrium contact angles with their standard deviations.

2.5.3 Analysis of surface topographical variation of membranes by AFM

Skin surface topographies of the Ps-nRGO composite UF membranes were analyzed by using an AFM instrument (NT-MDT SOLVER next, Russia). Quantitative informations were extracted from the AFM three-dimensional topographies as taken in the semi-contact mode. Small squares of the prepared membranes (approximately 1 cm^2) were cut and glued on a metal substrate. The rectangular cantilever NSG 10 (NT-MDT, Russia) employed for scanning purpose was made out of Si_3N_4 with a spring constant of 11.8 N/m, typical resonance frequency of 240 kHz and a nominal tip apex radius of 10 nm with high aspect ratio. The scanning was done on a 20 µm×20 µm area of the membranes in air, at an ambient temperature with a scanning frequency of 0.1Hz. The scanned region was flattened using a second order polynomial to remove curvature and slope from the image and then the resulting best fit was subtracted from the image. For image acquisition and evaluation of surface roughness parameters of the membranes NOVA-P9 software was used.

2.5.4 Morphological investigation of membranes by SEM

The morphological analyses, through SEM, of the Ps-nRGO composite UF membranes were carried out using CamScan–CS3200LV, UK. To make the membranes electrically conducting, the membrane samples (without support polyester fabric) were fractured in liquid nitrogen into smaller sized strips and sputter coated on the cross-sectional layer with gold-palladium alloy for 100 seconds at a current of 15 mA. The acquisition of cross-sectional images of the membranes was done in secondary electron mode at an acceleration voltage of 15 kV and 1000X magnification.

2.5.5 Evaluation of thermal stability of Ps-nRGO composite UF membranes

The thermal degradation process as monitored through the change of mass as a function of temperature, for the Ps-nRGO composite UF

membranes were investigated by employing thermogravimetric analyzer (Mettler-Toledo TGA/DSC 1 with STAR^e software, Switzerland). The analysis was conducted within a temperature range of 30-600^{o}C at a heating rate of 10^{o}C/min. A continuous flow of nitrogen gas was monitored in the test environment for an inert atmosphere.

2.5.6 Determination of mechanical stability of Ps-nRGO composite UF membranes

Measurement of mechanical stability of the Ps-nRGO composite UF membranes were carried out with a universal tensile testing machine (Hemetek Techno Instrument, model LRX Plus, India), at 25°C with a relative humidity of 40-50%. A constant deformation rate of 100 mm/min was controlled during the analysis. For analysis, dumb-bell shaped specimens of the membrane samples with length of 4 cm and width of 0.6 cm were employed. Tensile strength (TS) and percent elongation at break (EB) were calculated for the membranes in duplicates, using the NEXYGEN plus software.

2.6 Cross-flow permeation study of Ps-nRGO composite UF membranes

2.6.1 Measurement of pure water permeability of membranes

Pure water permeability measurements of the Ps-nRGO composite UF membranes were conducted in a UF test skid at a transmembrane pressure of 1 bar at room temperature. The steady state pure water permeability (PWP) was determined in terms of liter per square meter per day (LMD) by direct measurement of the permeate flow. The PWP (L.m^{-2}day^{-1}) through a membrane area (A, in m^2) was calculated as the volume (V, in L) collected during a time period (T, in day) and expressed by PWP = V/A×T. Prior to all UF test experiments, membranes were initially subjected to undergo compaction for 1 hour in water at standard UF test conditions, to achieve stabilized performances of the membranes. The hydraulic compaction behavior of the Ps-nRGO composite UF membranes were evaluated in terms of compaction factor by comparing the % flux decline results of each membrane.

2.6.2 Evaluation of solute rejection behavior of membranes

All Ps-nRGO composite UF membranes were employed for cross-flow permeation experiments in a UF test skid, with an effective membrane area of 14.5 cm^2. Measurements were carried out using polyethylene glycol (PEG) with average molecular weight of 35 kDa and polyethylene oxide (PEO) with average molecular weight of 100 kDa. The test solutions were prepared by dissolving pre-weighed amounts of PEG or PEO

in distilled water at a concentration of 200 ppm and solute rejection studies were carried out at a transmembrane pressure of 1 bar at room temperature. The concentration of PEG/PEO in both feed and product were measured by analysing the total organic carbon (TOC) content of the samples using TOC analyser (ANATOC, SGE analytical science, Australia).

3. Results & Discussions

3.1 Characterization of the synthesized nRGO

3.1.1 Raman studies on as-grown GO and nRGO

Structural transformations of GO into nRGO, through hydrazine induced chemical reduction pathway was analyzed by the Raman spectroscopic technique.

In the Raman spectra of GO and nRGO (Fig. 1), the D band, attributed to the structural defects or disorderness in the lattice structure, appears at 1356.2 cm^{-1} (FWHM:181.2 cm^{-1}) and 1343.5 cm^{-1} (FWHM:95.1 cm^{-1}), respectively and the G band, attributed to the first-order scattering of the E_{2g} vibrational mode in the graphite sheet, appears at 1575.5 cm^{-1} (FWHM:139.1 cm^{-1}) and 1579.9 cm^{-1} (FWHM:81.9 cm^{-1}), respectively.[46,47] A weak 2D band, observed at 2669.7 cm^{-1} is due to second order phonon process. It is observed that after being reduced, the D band becomes distinctively more intense as compared to the G band. The ratio of the integrated intensity of the D band to the integrated intensity of the G band (I_D/I_G) is markedly increased from 0.91 for GO to 1.18 for nRGO. This phenomenon could be explained by the formation of new and smaller sized abundant sp^2 domains during the reductive transformation process of exfoliated GO into nRGO. The restoration of the conjugated graphene network could be attributed to the proposed mechanism of Stankovich et al.,[48] where the oxirane rings of the GO sheets get preferentially converted into hydrazino alcohols through ring-opening reaction as induced by the reducing agent and then react further to form an aminoaziridine moiety with subsequent thermal elimination of diimide to form the sp^2 domains.[49] The reduction in FWHM values in the D band as well as G band for nRGO as compared to GO indicate that there is less disordered sites in the structure of the former species. The in-plane crystallite size, La of the nRGO is evaluated from a relation given as $La = (2.4\times10^{-10}) \lambda_{laser}^4 (I_G/I_D)$,[50] where the pre-factor derived by employing 532 nm as λ_{laser} is 19.22 (the pre-factor value is in contrast to the commonly used value of 4.4,[51]) and I_G/I_D implies the ratio of the intensity of the G band to the D band. The values of La for the synthesized GO and nRGO are found as 20.94 and 16.34 nm, respectively.

3.1.2 XPS studies on nRGO

The C-1s XPS core-level spectrum of the synthesized nRGO is presented in Fig. 2a, where curve fitting and deconvolution of the spectrum yields four separated spectra with different BE values (Table 1) for C atoms residing in various chemical environments. The intense component peak of the deconvoluted C-1s spectrum appeared at the lowest BE of 284.6 eV (FWHM: 1.55 eV) is ascribed to the nonoxygenated ring C of C–C or C–H. The broader and less intense peak appearing at BE of 286.5 eV (FWHM: 2.58 eV) refers to the C of C–OH functional groups.[52] Further, a much broader and shoulder peak appearing at the highest BE of 289.2 eV with respective FWHM of 4.39 eV refers to the carboxylate C of HO–C=O functional groups, residing at the edges of GO and remained unaffected during reduction process by hydrazine.[53] Additionally, a peak with BE of 285.8 eV (FWHM: 1.54) is also found, which implies the existence of some incorporated N in the lattice structures of nRGO due to the reaction of hydrazine with carbonyl groups of GO.[54] The deconvoluated O1s XPS spectra (Fig. 2b) of the more surface specific element O (the O1s photoelectron kinetic energies are lower than those of the C1s and so the sampling depth of O1s is smaller) reveal that the oxygen in nRGO is existed in two different electronic states. The less intense peak at lower BE of 530.1 eV (FWHM: 1.39 eV, Peak area: 3.37%) is assigned to the contribution of the O of HO–C=O functional groups and the broad and intense peak at higher BE of 533.2 eV ((FWHM: 3.62 eV, Peak area: 96.63%) is ascribed to the O of C–OH functional groups.[55]

Evaluation of areas (Table 1) of constituent peaks for C-1s and O-1s reveal that a significantly larger proportion of different surface oxygenated functional groups of nRGO, located at different sites of its edge and basal plane, existed in the form of hydroxyl and carboxylic acid groups.

3.1.3 XRD analysis on GO and nRGO

Diffraction peaks corresponding to (002) plane of GO and nRGO, appeared to be broad and symmetric that centered at 19.54° and 24.24° (Fig. 3a and 3b), respectively, signify the formation of stacked few-layers of the reduced graphene oxide. The interlayer spacing (d_{002}) of GO is evaluated as 0.454 nm. However, the adopted reduction process relevantly lowers the d_{002} of nRGO, which is evaluated as 0.367 nm. The shifting of d_{002} to a lower value, resulting in such low basal placing of nRGO is attributed to the absence of residual oxygenated functional groups at the basal planes, indicating intense reduction of the epoxide sites of GO.[56] This also indicates subsequent presence of different oxygenated functional groups at the edges of the nRGO. Thus, it can be assumed that the

numerous spatial ways through adjacent basal planes residing in the stacked few-layers of nRGO can serve as hydrophobic channels for fluid transport.[57] The average crystallite sizes for the nRGO, determined using Debye-Scherrer's equation range from 4 - 8 nm. A Lorentzian fit of the peak corresponding to the (002) reflection and use of the Scherrer formula provide the estimation of average number of layers as ~ 16, existing in the synthesized nRGO.

3.2 Characterization of the Ps-nRGO composite UF membranes

3.2.1 Investigation of structural features of Ps-nRGO composite UF membranes

The FTIR spectral analyses of the Ps-nRGO composite UF membranes, acquired in the specified regions of 800-1550 and 2750-3750 cm^{-1} are shown in Fig. 4a and 4b, respectively. The most significant absorption bands appeared in the FTIR spectrum of the membranes are: ~1149 and ~1294 cm^{-1}(symmetric and asymmetric stretching of O=S=O from diaryl sulfone groups) respectively; ~834 cm^{-1} (C-H stretching from Ar); ~1489 cm^{-1} (asymmetric vibration attributed to C-H from methyl groups) and ~1170 cm^{-1} (stretching vibration of etheric bond of Ar-O-Ar of Ps).[58] The peaks at ~2930 and ~2870 cm^{-1} refer to the asymmetric and symmetric stretching vibrations of C-H, respectively. The broad absorption band appearing at ~3420 cm^{-1} refers to the O-H stretching of the hydroxyl groups due to presence of inherent moisture in the membrane matrices. The non-shifting of characteristic absorption bands in Ps-nRGO composite UF membranes corroborate the fact that impregnation of nRGO at increasing weight fraction from 1 to 8 w/w% of Ps doesn't affect the structural features of the base matrix. Thus, the FTIR analysis reveals that the nRGO, due to its structural features exerts only weak chemical affinity to the surrounding polymer network and reside through physical entrapment within the Ps matrix, on their impregnation.

A further study on surface chemistry of the selective membranes, (Ps UF and Ps-nRGO UF-2), was conducted by analyzing the deconvoluated C-1s (Fig. 5a and 5b, respectively) and O-1s (Fig. 6a and 6b, respectively) core level XPS spectra. The intense and major component peak of the deconvoluated C-1s spectra is attributed to C–C or C–H bonds of the alkyl and aromatic chains of the polymer network of Ps UF and Ps-nRGO UF-2 (appearing at BE of 284.7 eV,[59,60]) with an invariable FWHM of about 1.93 eV. But, there is a percentage decline in the concerned peak area by 4.77%, from Ps UF to Ps-nRGO UF-2 (Table 2). This decrease is compensated by an increase of 9.54% in the relative peak area for the broader peak, appeared at BE of 286.1 eV, assigned to the carbon in –C–O– structures. It could be the

result of reinforcement of nRGO in Ps matrix of the Ps-nRGO UF-2, which further suggests that nRGO with its retained oxygen-containing functionalities contribute in enhancing the extent of polar sites in Ps membrane surface. The deconvoluated O-1s core level XPS spectra of the Ps UF and Ps-nRGO UF-2, respectively, indicate the presence of oxygen in two different chemical states. The bigger peaks at lower BE of 531.3 eV with FWHM of 2.20 eV for Ps UF and 2.25 eV for Ps-nRGO UF-2 refer to the collective contribution of presence of oxygen in O=S=O linkages of Ps backbone as well as the physiosorbed oxygen.[61] The percentage enhancement in the area under the curve for the peak of 531.3 eV from Ps UF to Ps-nRGO UF-2 is 5.01%. Thus it can be affirmed that presence of such enhanced content of polar oxygenated species on impregnation of nRGO seems to bring superior hydrophilic nature of the Ps-nRGO composite UF membranes over the pure Ps UF membrane. The smaller peak at higher BE of 533 eV, with FWHM of 2.02 eV for Ps UF and 2.18 eV for Ps-nRGO UF-2 is assigned to the oxygen in the structure of –C–O–, resulting out of the presence of oxygen-containing functionalities due to impregnation of nRGO.[62] The percentage decline in the area under the curve for the peak of 533 eV, by 7.35%, from Ps UF to Ps-nRGO UF-2 is due to the relative compensation of the earlier enhancement.

3.2.2 Evaluation of hydrophilic characteristics of Ps-nRGO composite UF membranes

The extent of hydrophilic nature of the membranes, as represented by the water contact angle values obtained on each of the membrane surface by the sessile drop method, is given in Fig. 7. It is observed that nRGO embedded Ps membranes exhibit more hydrophilic surface features than the pure Ps UF membrane. It is interesting to note that 1 w/w% loading of nRGO brings significant change in hydrophilic behavior of the membrane (Ps-nRGO UF-1) with a contact angle value of 70.7 ± 0.7^{o} compared to that of pure Ps UF membrane with contact angle value of 76.2 ± 1.1^{o}. The impregnation of nRGO at lower weight fraction influences the direction of migration and consequent dispersion of the nano-additive towards the skin surface of the membrane due to more affinity of them towards the non-solvent, water.[63] The presence of oxygenated functionalities in nRGO, as confirmed by the XPS analysis also supports the enhancement of hydrophilic behavior of the skin surfaces of the Ps-nRGO composite UF membranes. But, with further loading of nRGO, the change in water contact angle values (Ps-nRGO UF-2: 69.8 ± 0.8^{o}, Ps-nRGO UF-3: 68.1 ± 0.6^{o} and Ps-nRGO UF-4: 67.2 ± 0.9^{o}) were not pronounced. This feature can be attributed to the fact that at higher loading, the uniform distribution of the nRGO gets affected with a further impact in their presence within the skin

layers of the Ps matrix. An enhanced permeation behavior (discussed later) with modest change in hydrophilic character for these membranes, fabricated by employing nRGO at higher weight fractions, can be elucidated by the proposition that the aggregated nRGO reside onto the pore walls within the Ps matrix during the formation of the membranes and induce changes in hydrophilic characters of the porous pathways.[64]

3.2.3 Morphological analysis of Ps-nRGO composite UF membranes

Ultrafiltration membranes, fabricated following the technique of non-solvent induced phase inversion process, is known to consist of asymmetric porous structure where the pores formed at the skin surface are smaller in size as compared to the pores formed in the interior of the substructure. The porous structures usually vary in size, shape and density throughout the polymer matrix (i.e., from the dense skin surface to the more porous subsurface) of the membrane. Such variations in membrane morphology depend on the phase behavior of the polymer dope solutions as well as the rate of the non-solvent's indiffusion and the solvent's outdiffusion during phase separation process.[65] Thus, it can be anticipated that presence of a nanostructured additive with hydrophilic or hydrophobic functionalities can influence the mechanism of formation of nanocomposite UF membranes.

In our attempt to investigate the porous structures of the Ps-nRGO composite UF membranes, the cross-sectional SEM images, presented in Fig. 8 are analyzed. A visual observation of the size, shape and density of the finger-like pores, residing underneath the skin layer, for the membranes Ps UF (Fig. 8a), Ps-nRGO UF-1 (Fig. 8b) and Ps-nRGO UF-2 (Fig. 8c) reveal that all the membranes maintain a dense skin layer with roughly similar finger-like porous nature associated with fine porous walls. As illustrated in earlier studies,[66,67] the formation of membranes with finger-like pores comprise of few consecutive interdependent stages. Initially, a dense polymer layer is formed as a skin layer at the interface between the cast polymer solution and the gelling medium with concurrent existence of a polymer-rich and a polymer-lean phase underneath the nascent skin layer. However, during the process of phase separation, the nascent skin experiences shrinkage and resultant stress, which if not relieved through stress-relaxation, results in rupture of the skin layer and initiation of growth for the finger-like pores. The growth of the finger-like pores are propagated by the movement of the polymer solution through the channel, forming a pear shaped porous confinement. In our investigation, it is observed that the size, shape as well as density of the finger-like pores change when nRGO is impregnated at higher weight fraction (Ps-nRGO UF-4). It could be possible that nRGO at lower weight fractions (up to 2 w/w%) with

considerably better uniformity in distribution within the polymer matrix may reduce the stress generated in the skin layer of the cast polymer during phase inversion stage and delay the initiation process for growth of the finger-like pores. But, at higher weight fraction (beyond 2 w/w%), due to enhanced particle density as well as greater aggregation of the nRGO, there may be significant differences in the interfacial tension which could result in comparatively faster initiation of fingering leading to formation of bigger and more macro-voids, as evident in Fig. 8e. As seen in Fig. 8c, aggregation of the nanofillers is initiated at 2 w/w% loading of nRGO and the extent is increasing with further loading up to 4 w/w% (Fig. 8d). Surprisingly, the aggregates are vanished at 8 w/w% (Fig. 8e) loading of nRGO which can be attributed to formation of defective membrane having more number of bigger macro-voids. It is important to note that though the aggregate formation is just initiated at 2 w/w% (Fig. 8c) loading of nRGO, but, the extent of fingering is less compared to the pure Ps UF (Fig. 8a) and Ps-nRGO UF-1 (Fig. 8b), which can further be attributed to a delayed penetration of the nonsolvent into polymer matrix during gelling of the polymer.

Thus, the impregnation of nRGO at varying weight fractions tune the membranes porous morphology profoundly as the mechanism of formation of the pores get influenced by the presence of the nano-additive.

3.2.4 Topographical analysis of skin surfaces of Ps-nRGO composite UF membranes

Topographical variations in the skin surfaces of Ps-nRGO composite UF membranes were evaluated through AFM analysis. The 2D AFM images of all the membrane surfaces with the respective height histograms are shown in Fig. 9. It is observed that the surface topographies of the membranes with associated roughness parameters vary significantly from a relatively smooth surface profile for the Ps UF membrane to progressively rough surfaces for membranes with higher impregnation of nRGO (Fig. 10).

The average surface roughness (R_a) and root mean square roughness (R_q) of the pure Ps UF membrane was found to be 9.49 and 11.74 nm, respectively. However, the surface roughness was found to increase with enhanced impregnation of nRGO in the polymer matrices with subsequent effect on distribution in the skin surfaces through varying dispersion of nRGO. This is obvious from the gradual increase of R_a and R_q values for nRGO embedded Ps based UF membranes, namely Ps-nRGO UF-1, Ps-nRGO UF-2, Ps-nRGO UF-3 and Ps-nRGO UF-4, which were found to be about 16.08, 18.12, 28.69 and 33.87 nm, respectively and 19.71, 23.21, 35.43 and 45.55 nm, respectively. With such enhanced roughnesses of the surfaces, the nanocomposite membranes possess higher effective skin surface area for more efficient

contact of water. The R_{10z}, which is the difference in height between the average of the five highest peaks and the five lowest valleys relative to the mean plane, signifies the contrast between the heights and depths of extreme peaks and valleys that may occasionally be present on the surface, due to uneven distribution of nanomaterials in the surface. For fabrication of the membranes, Ps-nRGO UF-3 and Ps-nRGO UF-4, when the nRGO content turns as high as 4 and 8 w/w% of Ps, the particle density of nRGO in the polymer dope solution becomes extremely high causing aggregation of the nRGO and results in abrupt increase of their surface areas. Such aggregation can also influence the phase separation processes during formation of the nanocomposite membranes and may lead to inhomogeneous distribution of the clusters of nRGO with concurrent nonhomogenity in surface as well as in bulk of the membrane matrices. Impregnation of nRGO at 4 w/w% (Ps-nRGO UF-3) results in larger voids in the membrane matrices due to formation of the clusters, which is reflected through the surface roughness parameters. In spite of having higher roughness values, the R_{10z} becomes lower i.e., 16.53 nm for Ps-nRGO UF-3 as compared to 54.69 nm (Ps-nRGO UF-1) and 56.29 nm (Ps-nRGO UF-2). However, impregnation of nRGO at 8 w/w% (Ps-nRGO UF-4) results in presence of aggregated nRGO within the Ps skin layer of the membrane, where the average heights of the peaks due to such nRGO-polymer aggregates enhances the value of R_{10z} (88.96 nm) abruptly.

3.2.5 Study of thermal stability of Ps-nRGO nanocomposite UF membranes

The results of TGA-investigation for Ps and Ps-nRGO composite UF membranes obtained with different nRGO contents (1, 2, 4 and 8 w/w %) is reported in Table 2 and Fig. 11. The onset degradation temperature (T_d) has increased from 507.8^{o}C (Ps UF) to 513.5^{o}C (Ps-nRGO UF-1) and 512.9^{o}C (Ps-nRGO UF-2), which is attributed to the presence of well dispersed nRGO sheets within the Ps matrix. It is assumed that the increase in thermal stability happens by suppressing the flexibility and mobility of the polymer chains due to uniform distribution of the nano-additive within the Ps matrices. However, the onset degradation temperature decreases with further loading of nRGO beyond 2 w/w % for Ps-nRGO UF-3 (509.7^{o}C) and Ps-nRGO UF-4 (510.4^{o}C), which is expected to happen because of aggregation of nRGO at higher loadings leading to relaxation of the restriction in polymer chain mobility.[68] More importantly, the extent of overall mass loss is maximum (57.61 %) in case of Ps membrane without having any nRGO in it. The extents of mass loss in all nanocomposite UF membranes are comparatively lower (from 51.56 to 54.01 %) because of existence of more proportion of nRGO (which is thermally stable

due to absence of labile oxygen containing functionalities) in the membrane matrix.

3.2.6 Analysis of mechanical stability of Ps-nRGO composite UF membranes

Evaluation of the membranes tensile strength and percentage elongation at break, shown in Fig. 12 and Table 3, reveal the effectiveness of the nRGO as nanostructured reinforcement material in bringing better mechanical stability for nanocomposite Ps UF membranes. It is observed that the tensile strength enhances from 2.94 MPa (Ps UF) to 3.33 MPa (Ps-nRGO UF-1) and further to 3.42 MPa (Ps-nRGO UF-2) with incorporation of 1 and 2 w/w% of nRGO in the Ps matrix. The suitability of nRGO as potential reinforcement material is attributed to its higher surface area and aspect ratio. Due to absence of the oxygen containing functionalities, as possible interactive bridging sites of nRGO, the nanomaterials presumably reside apart from each other during their dispersion in the precursor dopes at lower weight fractions.[69] Further, since nRGO experiences a weak interaction with the polymer (as discussed during structural analysis by FTIR), the possibility of the former to act as cross-linker and subsequent formation of higher molecular weight chains also get diminished. The polymeric chains penetrate in between the nRGO sheets resulting in a better uniform distribution of the reinforcement material within the polymer network. Thus, the increase of tensile strength can be ascribed to the fact that there is a effective load transfer from the stretched polymeric chains to the well dispersed nRGO.[70] However, there is a decline in the tensile strength with further impregnation of nRGO in Ps-nRGO UF-3 and Ps-nRGO UF-4. The decrease in mechanical strength, as noticed beyond 2 w/w% of nRGO impregnation in the Ps matrix, is attributed to the aggregation effect of nRGO, which could further lead to non-uniform distribution of the material in the membrane matrices resulting in less efficient load transfer from the continuous phase (Ps) to the disperse phase (nRGO).

Generally, the addition of filler decreases the ductility of polymers, e.g., elongation at break.[71] Similar observation has also been obtained in our case. The percentage elongation at break for the nanocomposite UF membranes decrease from Ps UF (36.83%) to Ps-nRGO UF-1 (32.41%) and further to Ps-nRGO UF-2 (30.04%) with increasing the content of nRGO. These results imply that the membranes elasticity decline with progressive impregnation of nRGO into the Ps matrices. The reduced elongation at break often means a reduced energy to break. However, surprisingly, the elongation at break in the present case increases on further loading of nRGO beyond 2 w/w%. The behavior can be explained by the fact that the increase in stress levels via reinforcement is not dominant over the reduction in deformation at higher loadings,

which is in contrary to the usual findings for nanocomposites.[72]

3.3 Performance studies of Ps-nRGO composite UF membranes

Cross-flow water permeation experiments performed with Ps-nRGO composite UF membranes reveal that impregnation of nRGO with the increasing weight fraction leads to better PWP compared to the pure Ps UF membrane. The rejection pattern towards the neutral organic solutes like PEG and PEO, carried out using the membrane samples, are presented in Fig. 13. It is noticed that with impregnation of nRGO at smaller weight fraction (1 to 2 w/w% of Ps) in the Ps polymer matrix, the solute rejection properties of the UF membranes get improved as compared to the pure Ps UF membrane. It is also observed that the membrane with a loading of 2 w/w% of nRGO (Ps-nRGO UF-2) achieves a promising MWCO of 30 kDa, as the membrane exhibited 92% rejection with a feed containing 200 ppm of PEG of Mw 35 kDa. Interestingly, the PWP obtained from the respective membrane (Fig. 14) turn out to be better than that of pure Ps UF membrane of higher MWCO (100 kDa), which reflect the prevailing over of the trade off between flux and selectivity. Both, a higher rejection (> 90%) towards solute of higher Mw, i.e., PEO (100 kDa) and simultaneous progressive increment in solvent fluxes are maintained by all the membranes, even with loading of nRGO at higher weight fractions. But, the rejection performances for the low Mw solute, i.e., PEG 35 kDa, deteriorates with an enhancement of nRGO content beyond 2 w/w% i.e. from 4 to 8 w/w%, in the membrane matrices. Thus, nRGO embedment in Ps host matrix at an optimum proportion leads to a membrane with better flux and improved rejection qualities. This kind of macroscopical variations is attributed to the change in several microstructural and physicochemical features of the nanocomposite UF membranes. Better solute rejections for Ps-nRGO UF-1 and Ps-nRGO UF-2, over the pure Ps UF, imply that there may be formation of finer pores on the skin surfaces of the former membranes due to controlled phase inversion process, as discussed during morphological analysis of the membranes by SEM. However, the concurrent increase in PWP of the respective nanocomposite UF membranes corroborates the fact that there could be an enhancement in the extent of nanosized permeating channels for faster transport of the solvent in addition to the improvement in their hydrophilic behaviors as discussed earlier.

Thus, it is worthy to substantiate the enhanced permeation ability of the Ps-nRGO composite UF membranes by the additional and facilitated transport of water caused by the atomically smooth interconnected interlayers (as novel pathways for water permeation) offered by nRGO impregnated in the Ps matrices. Like the

case of hydrophobic CNTs,[73] it can also be expected that numerous nRGO with interlayer spacing of 0.37 nm, may collectively provide such empty regions as nano-confinements for the solvent molecules (kinetic diameter of water 0.26 nm)[74] to enter preferentially and get ordered during hydraulic permeation process, narrowing their interaction energy distribution with concomitant effect in reduction of their free energy.[75] However, the narrow entrance of the nano-confinements restricts the transport of solute molecules (PEG/PEO) because of size exclusion phenomena. Furthermore, due to the hydrophobic nature of the walls (basal planes) of permeating channels of nRGO, serving as electrostatically frictionless pathways, the water molecules experience less dragging force during their transport.[76,77] Thus, with reference to the concept of slip flow theory,[78] the above fact can be attributed as a cause for unconstrained hydraulic permeability with restoration of momentum, for the Ps-nRGO composite UF membranes. On a further note of explanation, the enhanced permeation ability of the membranes is ascribed to the topographical effects on impregnation of nRGO with progressive higher weight fraction leading to increase in effective surface area of the membranes, which is evident from the study of surface roughness analysis.

The formation of phase inversion membranes is also known to be controlled by thermodynamic as well as kinetic variations resulting either instantaneous or delayed demixing during precipitation of the casting polymer solutions.[79] It was mentioned in earlier studies[80] that instantaneous demixing generally leads to membrane with a highly porous substructure and a finely porous thin skin layer, whereas in contrast, a delayed demixing results in a membrane comprising porous substructure with a dense skin layer. Recent studies on nanocomposite asymmetric membranes have attempted to explain that impregnation of a novel nanomaterial like GO, having different hydrophilic functionalities facilitates the rate of diffusive mass exchange between solvent and non-solvent during the phase inversion process of the polymer, consequently resulting in increased porosities as well as larger pore channels, further affecting the rejection and flux behavior of the UF membranes.[81] However, in comparison to those studies, here, in our attempt to impregnate nRGO as nano-additive in Ps matrices, the former having a reduced extent of oxygen containing functionalities exhibit less interaction ability with the solvent, NMP and also a low affinity towards the non-solvent, water. Such interaction behavior of the nano-additive favors the solvent's outdiffusion from the cast polymer and simultaneously unfavors the non-solvent's indiffusion into the cast polymer during phase inversion stage in the gelling medium. Thus, the thermodynamic stability of the Ps-nRGO dope solution remains reasonably uninterrupted, unlike the case with the

hydrophilic counterpart of nRGO (i.e., GO). This may induce comparatively slower diffusion kinetics during the phase separation process, which in turn affect the membrane morphology by reducing the porosities in the skin surfaces. The hydrophilic additive, PVP is known to reduce the miscibility of casting solutions with non-solvent, which results in thermodynamic enhancement for phase separation of the polymer, Ps and also stimulates the increase in viscosity of the casting solution, which induces kinetic inhibition against the phase separation process.[82] However, a lower degree of chemical affinity of nRGO towards the PVP may enhance the rate of outdiffusion of the later in the non-solvent medium, which could generate more number of micro or macro-voids in the substructure of the asymmetric membrane matrices. It can be assumed that impregnation of the nano-additive, nRGO brings synergism in the demixing process by balancing the inter-diffusion of solvent and non-solvent as well as pore former and non-solvent, during phase inversion stage of membrane fabrication.

In porous asymmetric membranes, the occurrence of compaction preferentially happens in the macro-void regions over the micro-void regions of the polymer matrix. Thus presence of larger macro-voids irreversibly tailors the membrane morphology to be more compactable under hydraulic pressure.[83] Albeit, the cluster formation leads to an abrupt increase of effective surface area of the membranes with resultant enhanced solvent permeation, the extent of flux decline for the membranes (Fig. 15) corroborates the above facts. The enhanced free-volume area with formation of larger macro-voids in the membranes and the change in pore structure, presumably due to the increasing segmental gap between the polymer chains through relaxation effect, as induced by the clusters of nRGO may simultaneously affect the solute rejection behavior of the membranes in adverse manner.

4. Conclusions

Ps-nRGO composite UF membranes with varying proportions of nRGO were prepared using phase inversion technique and characterized using various instrumental techniques. The flux and solute rejection studies were carried out using solutions of different molecular weight PEG and PEO. It was observed that an optimum loading of nRGO (2 w/w% of Ps) resulted in membranes with MWCO of 30 kDa without compromise in flux as compared to the pure polysulfone membranes with MWCO of 100 kDa. In addition, the optimum loading of nRGO (2 w/w% of Ps) resulted membranes with better thermal and mechanical stability. This essentially opens up newer ways to develop ideal membranes with improved flux, optimum selectivity and reasonable thermal and mechanical stability.

Notes and references

1 P. K. Stoimenov, R. L. Klinger, G. L. Marchin and K. J. Klabunde, *Langmuir*, 2002, **18**, 6679–6686.

2 P. Jain and T. Pradeep, *Biotechnology and Bioengineerin*g, 2005, **90**, 59–63.

3 F. Furno, K. S. Morley, B. Wong, B. L. Sharp, P. L. Arnold, S. M. Howdle, R. Bayston, P. D. Brown, P. D. Winship and H. J. Reid, *Journal of Antimicrobial Chemotherapy*, 2004, **54**,1019–1024.

4 J. R. Morones, J. L. Elechiguerra, A. Camacho, K. Holt, J. B. Kouri, J. T. Ramirez and M. J. Yacaman, *Nanotechnology*, 2005, **16**, 2346–2353.

5 W. K. Son, J. H. Youk, T. S. Lee and W. H. Park, *Macromolecular Rapid Communications*, 2004, **25**, 1632–1637.

6 E. Bae and W. Choi, *Environmental Science and Technology*, 2003, **37**, 147–152.

7 E. A. Ayuso, A. G. Sanchez and X. Querol, *Water Research*, 2003, **37**, 4855–4862.

8 B. H. Jeong, E. M. V. Hoek, Y. Han, A. Subramani, X. Huang, G. Hurwitz, A. K. Ghosh and A. Jawor, *J. Membr. Sci.*, 2007, **294**, 1–7.

9 Y. H. Li, S. Wang, J. Wei, X. Zhang, C. Xu, Z. Luan, D. Wu and B. Wei, *Chemical Physics Letters*, 2002, **357**, 263–266.

10 Y. H. Li, S. Wang, Z. Luan, J. Ding, C. Xu and D. Wu, *Carbon*, 2003, **41**, 1057–1062.

11 Y. H. Li, S. Wang, X. Zhang, J. Wei, C. Xu, Z. Luan and D. Wu, *Materials Research Bulletin*, 2003, **38**, 469–476.

12 X. Peng, Z. Luan, J. D., Z. Di, Y. Li and B. Tian, *Materials Letters*, 2005, **59**, 399–403.

13 A. Srivastava, O. N. Srivastava, S. Talapatra, R. Vajtai and P. M. Ajayan, *Nature Materials*, 2004, **3**, 610–614.

14 S. Kar, R. C. Bindal, S. Prabhakar, P. K. Tewari, K. Dasgupta and D. Sathiyamoorthy. *Int. J. of Nuc. Des.*, 2008, **3**, 143–150.

15 M. S. Diallo, S. Christie, P. Swaminathan, J. H. Johnson Jr. and W. A. Goddard III, *Environmental Science and Technology*, 2005, **39**, 1366–1377.

16 J. M. J. Frechet and D. A. Tomalia, Dendrimers and other dendritic polymers. New York: Wiley and Sons, 2001.

17 M. F. Ottaviani, P. Favuzza, M. Bigazzi, N. J. Turro, S. Jockusch and D. A. Tomalia, *Langmuir*, 2000, **16**, 7368–7372.

18 M. Arkas, D. Tsiourvas and C. M. Paleos, *Chemistry of Materials*, 2003, **15,** 2844–2847.

19 C. Z. S. Chen and S. Cooper, *Biomaterials*, 2002, **23**, 3359–3368.

20 L. Balogh, D. R. Swanson, D. A. Tomalia, G. L. Hagnauer and A. T. McManus, *Nano Letters*, 2001, **1,** 18–21.

21 L. Yan, S. Hong, M. L. Li and Y. S. Li, *Sep. and Puri. Tech.*, 2009, **66**, 347–352.

22 Z. Fan, Z. Wang, M. Duan, J. Wang and S. Wang, *J. Membr. Sci.*, 2008, **310**, 402–408.

23 J. S. Taurozzi, H. Arul, V. Z. Bosak, A. F. Burban, T. C. Voice, M. L. Bruening and V. V. Tarabara, *J. Membr. Sci.*, 2008, **325**, 58–68.

24 W. L. Chou, D. G. Yu and M. C. Yang, *Polymers for Advanced Technologies*, 2005, **16,** 600–607.

25 D. G. Yu, M. Y. Teng, W. L. Chou and M. C. Yang, *J. Membr. Sci.*, 2003, **225**, 115–123.

26 W. K. Son, J. H. Youk, T. S. Lee and W. H. Park, *Macromolecular Rapid Communications*, 2004, **25**, 1632–1637.

27 K. S. Novoselov, A. K. Geim, S. V. Morozov, D. Ziang, Y. Zhang, S. V. Dubonos, I. V. Grigorieva and A. A. Firsov, *Science*, 2004, **306**, 666.

28 R. R. Nair, H. A. Wu, P. N. Jayaram, I. V. Grigorieva and A. K. Geim, *Science*, 2012, **335**, 442.

29 D. R. Paul, *Science*, 2012, **335**, 413–414.

30 A. Enotiadis, K. Angjeli, N. Baldino, I. Nicotera and D. Gournis. *Small*, 2012, **8**, 3338–3349.

31 Y. Heo, H. Im and J. Kim, *J. Membr. Sci.*, 2013, **425–426**, 11–22.

32 Y. Zhao, Z. Xu, M. Shan, C. Min, B. Zhou, Y. Li, B. Li, L. Liu and X. Qian, *Sep. Purif. Technol.,* 2013, **103**, 78–83.

33 J. Zhang, Z. Xu, W. Mai, C. Min, B. Zhou, M. Shan, Y. Li, C. Yang, Z. Wang and X. Qian, *J. Mater. Chem. A*, 2013, **1**, 3101–3111.

34 Z. Wang, H. Yu, J. Xia, F. Zhang, F. Li, Y. Xia and Y. Li, *Desalination*, 2012, **299**, 50–54.

35 N. Wang, S. Ji, G. Zhang, J. Li and L. Wang, *Chem. Eng. J.*, 2012, **213**, 318–329.

36 N. Wang, S. Ji, J. Li, R. Zhang and G. Zhang. *J. Membr. Sci.*, 2014, **455**, 113–120.

37 D. Jiang, V. R. Cooper and S. Dai, *Nano Lett.*, 2009, **9,** 4019–4024.

38 C. Zhao, X. Xu, J. Chen and F. Yang, *J. Env. Che. Eng.*, 2013, **1**, 349–354.

39 C. Zhao, X. Xu, J. Chen, G.Wang and F. Yang, *Desalination*, 2014, **340**, 59–66.

40 A. Lerf, H. He, M. Forster and J. Klinowski, *J. Phys. Chem. B*, 1998, **102**, 4477-4482.

41 M. Majumder, N. Chopra and B. J. Hinds, *ACS Nano*, 2011, **5**, 3867–3877.

42 R. R. Nair, H. A. Wu, P. N. Jayaram, I. V. Grigorieva and A. K. Geim, *Science,* 2012, **335**, 442–444.

43 W. S. Hummers and R. E. Offeman, *J. Am. Chem. Soc.*, 1958, **80**, 1339.

44 D. C. Marcano et al., *ACS Nano*, 2010, **4**, 4806–4814.

45 X. Gao, J. Jang and S. Nagase, *J. Phys. Chem. C*, 2010, **114**, 832–842.

46 P. G. Ren, D. X. Yan, X. Ji, T. Chen and Z. M. Li, *Nanotechnology*, 2011, **22**, 055705.

47 G. Srinivas, Y. Zhu, R. Piner, N. Skipper, M. Ellerby and R. Ruoff, *Carbon*, 2010, **48**, 630–635.

48 S. Stankovich et al., *Carbon*, 2007, **45**, 1558–1565.

49 P. M. Lahti, *Tetrahedron Lett.*, **24,** 1983, 2339–2342.

50 M. A. Pimenta, G. Dresselhaus, M. S. Dresselhaus, L. G. Cancado, A. Jorio and R. Saitoe, *Phys. Chem. Chem. Phys.*, 2007, **9**, 1276–1291.

51 K. S. Subrahmanyam, S. R. C. Vivekchand, A. Govindaraj and C. N. R. Rao, *J. Mater. Chem.*, 2008, **18**, 1517–1523.

52 D. Yang, A. Velamakanni, G. Bozoklu, S. Park, M. Stoller, R. D. Piner, S. Stankovich, I. Jung, D. A. Field, C. A. Ventrice Jr. and R. S. Ruoff, *Carbon*, 2009, **47**, 145–152.

53 Y. Qiu, X. Zhang and S. Yang, *Phys. Chem. Chem. Phys.*, 2011, **13**, 12554–12558.

54 R. J. Waltman, J. Pacansky and C. W. Bates Jr., *Chem. Mater.*, 1993, **5**, 1799–1804.

55 H. Yang, F. Li, C. Shan, D. Han, Q. Zhang, L. Niu and A. Ivaska, *J. Mater. Chem.*, 2009, **19**, 4632–4638.

56 T. Tojo, K. Fujisawa, H. Muramatsu, T. Hayashi, Y. A. Kim, M. Endo, M. Terrones and M. S. Dresselhaus, *RSC Adv.*, 2013, **3**, 4161–4166.

57 J. Shen, G. Liu, K. Huang, W. Jin, K. R. Lee and N. Xu, *Angew. Chem. Int. Ed.*, 2015, **54**, 578–582.

58 S. I. Voicu, M. A. Pandele, E. Vasile, R. Rughinis, L. Crica, L. Pilan and M. Ionita, *Digest Journal of Nanomaterials and Biostructures*, 2013, **8**, 1389 –1394.

59 K. S. Kim, K. H. Lee, K. Cho and C. E. Park, *J. Membr. Sci.*, 2002, **199**, 135–145.

60 D. S. Wavhal and E.R. Fisher, *Desalination*, 2005, **172**, 189–205.

61 J. Hopkins and J. P. S. Badyal, *J. Polymer Sci. Part A: Polymer Chem.*, 1996, **34**, 1385 –1393.

62 X. Feng, N. Dementev, W. Feng, R. Vidic and E. Borguet, *Carbon*, 2006, **44**, 1203–1209.

63 B. M. Ganesh, A. M. Isloor and A. F. Ismail, *Desalination*, 2013, **313**, 199–207.

64 F. Jin, W. Lv, C. Zhang, Z. Li, R. Su, W. Qi, Q. H. Yang and Z. He, *RSC Adv.*, 2013, **3**, 21394–21397.

65 P. van de Witte, P. J. Dijkstra, J. W. A. van den Berg and J. Feijen, *J. Membr. Sci.*, 1996, **117**, 1–31.

66 H. Strathmann and K. Koch, *Desalination*, 1977, **21**, 241–255.

67 H. Strathmann, K. Koch, P. Aimar and R.W. Baker, *Desalination*, 1975, **16,** 179–203.

68 M. Ionita, A. M. Pandele, L. Crica and L. Pilan, *Composites: Part B*, 2014, **59**, 133–139.

69 S. T. Knauert, J. F. Douglas and F. W. Starr, *J. Polymer Sci.: Part B: Polymer Phy.*, 2007, **45**, 1882–1897.

70 A. Bhattacharyya, S. Chen and M. Zhu, *eXPRESS Polymer Letters*, 2014, **8**, 74–84.

71 D. R. Paul and L. M. Robeson, *Polymer*, 2008, **49**, 3187–3204.

72 C. A. Crock, A. R. Rogensues, W. Shan and V. V. Tarabara, *Water Research*, 2013, **47,** 3984 –3996.

73 A. Striolo, *Nano Lett.*, 2006, **6**, 633–639.

74 J. E. ten Elshof, C. R. Abadal, J. Sekulic, S. Roy Chowdhury and D. H. A. Blank, *Microporous and Mesoporous Materials*, 2003, **65,** 197–208.

75 A. Noy, H. G. Park, F. Fornasiero, J. K. Holt, C. P. Grigoropoulos and O. Bakajin, *nanotoday*, 2007, **2,** 22-29.

76 D. R. Dreyer, S. Park, C. W. Bielawski and R. S. Ruoff, *Chem. Soc. Rev.*, 2010, **39**, 228–240.

77 Y. Han, Z. Xu and C. Gao, *Adv. Funct. Mater.,* 2013, **23**, 3693–3700.

78 G. Hummer, J. C. Rasaiah and J. P. Noworyta, *Nature*, 2001, **414,**188-190.

79 Y. Yun, P. Le-Clech, G. Dong, D. Sun, Y. Wang, P. Qin, Z. Chen, J. Li and C. Chen, *J. Membr. Sci.,* 2012, **389**, 416–423.

80 D. M. Wang, F. C. Lin, J.C. Chiang and J. Y. Lai, *J. Membr. Sci.,* 1998*,* **141**, 1-12.

81 V. Vatanpour, S.S. Madaeni, R. Moradian, S. Zinadini and B. Astinchap, *Sep. Purif. Technol.*, 2012, **90**, 69–82.

82 B. Chakrabarty, A. K. Ghoshal and M. K. Purkait, *J. Membr. Sci.,* 2008*,* **315**, 36–47.

83 K. M. Persson, V. Gekas and G. Tragardh, *J. Membr. Sci.,* 1995, **100**, 155-162.

Figures

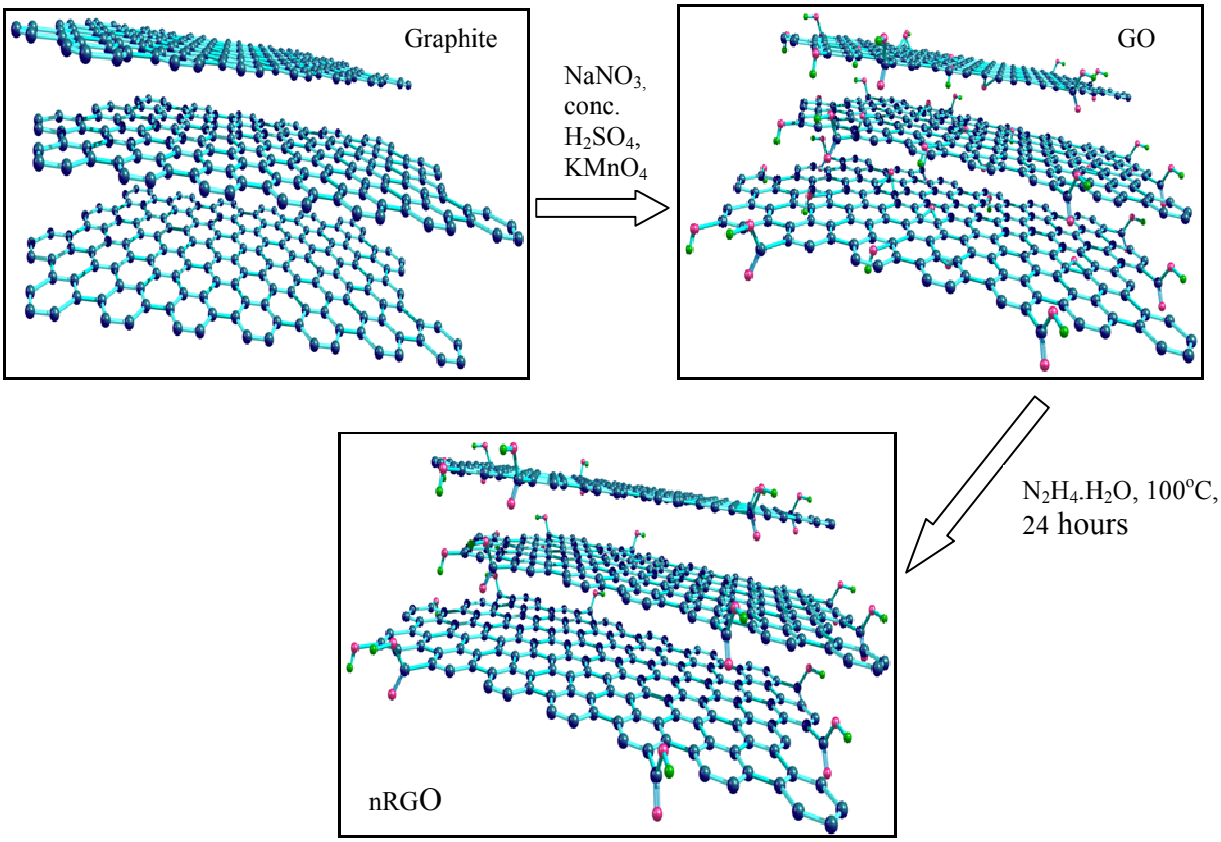

Scheme 1. Schematics of oxidation-reduction reaction for conversion of graphite in GO and nRGO.

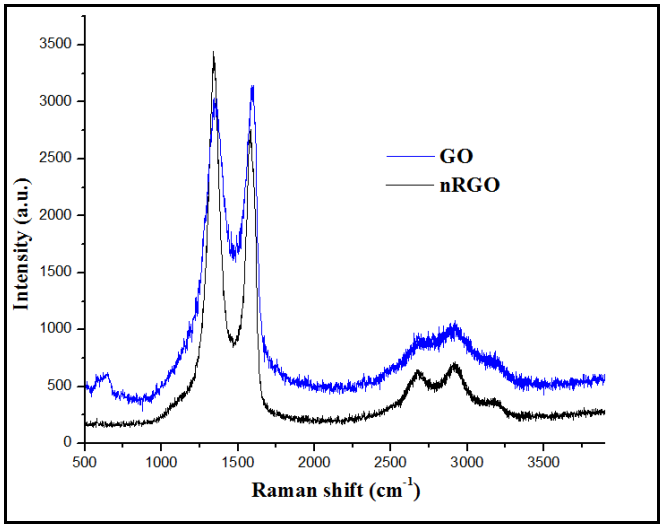

Fig. 1 Raman spectrum of GO and nRGO.

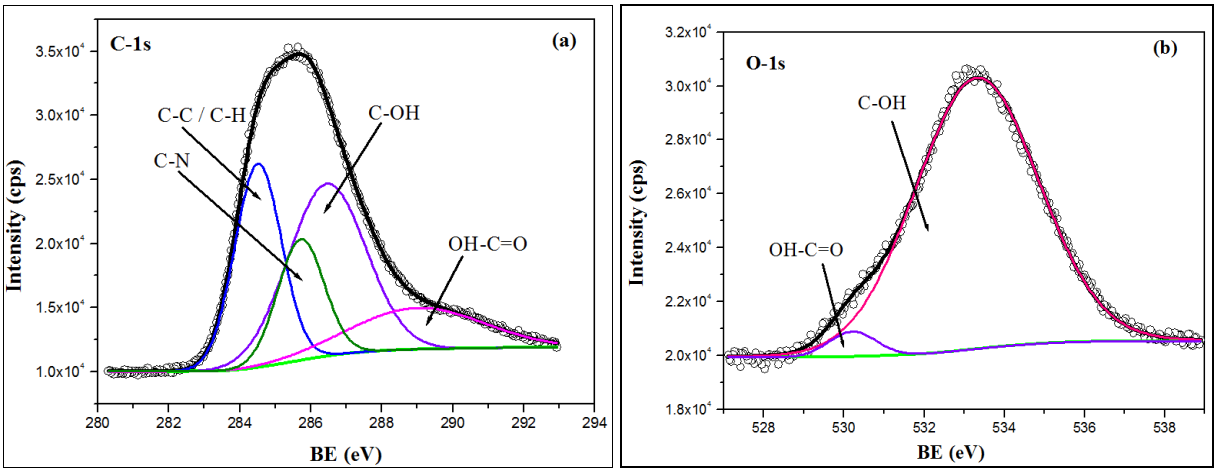

Fig. 2 High resolution XPS core level spectra, a) C-1s and b) O-1s of the synthesized nRGO (line with bullets: experimental data; solid line: curve fit of the experimental data).

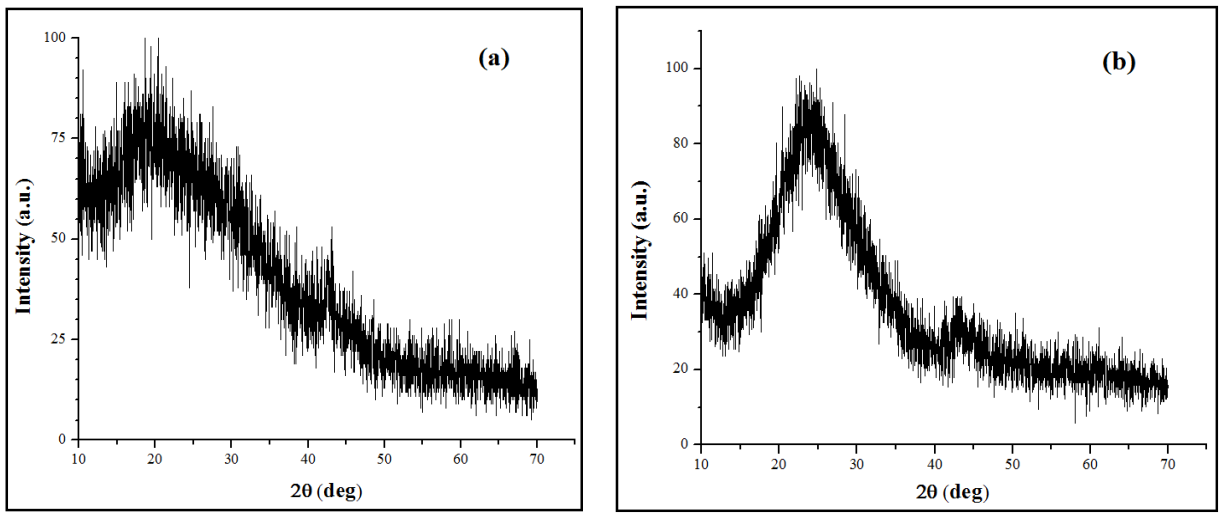

Fig. 3 XRD pattern of the synthesized, a) GO and b) nRGO.

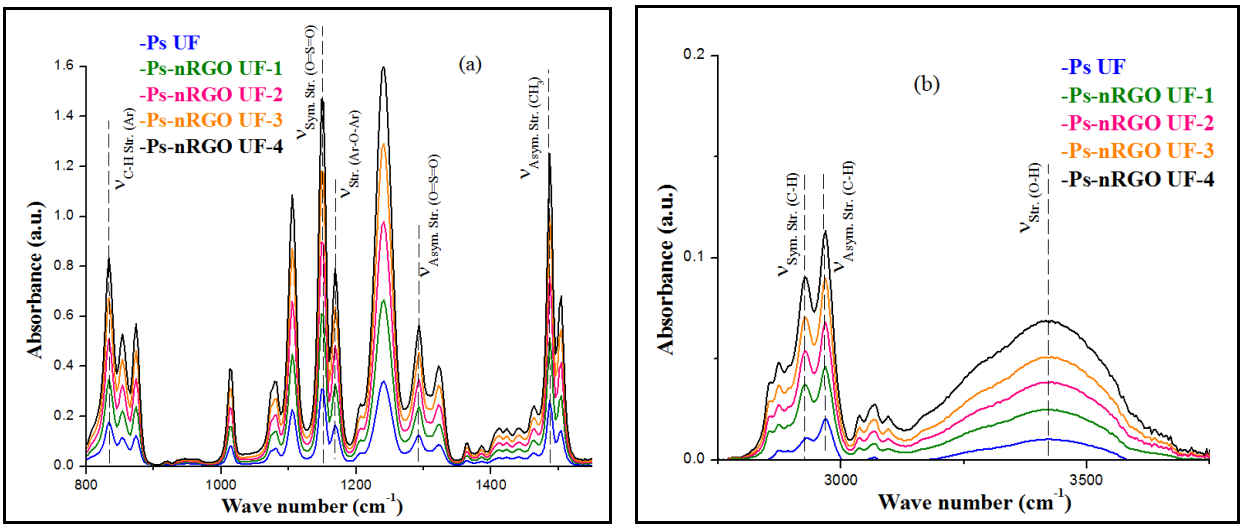

Fig. 4 ATR FT IR spectra a) 800-1550 cm^{-1} and b) 2750-3750 cm^{-1} of Ps UF and Ps-nRGO composite UF membranes.

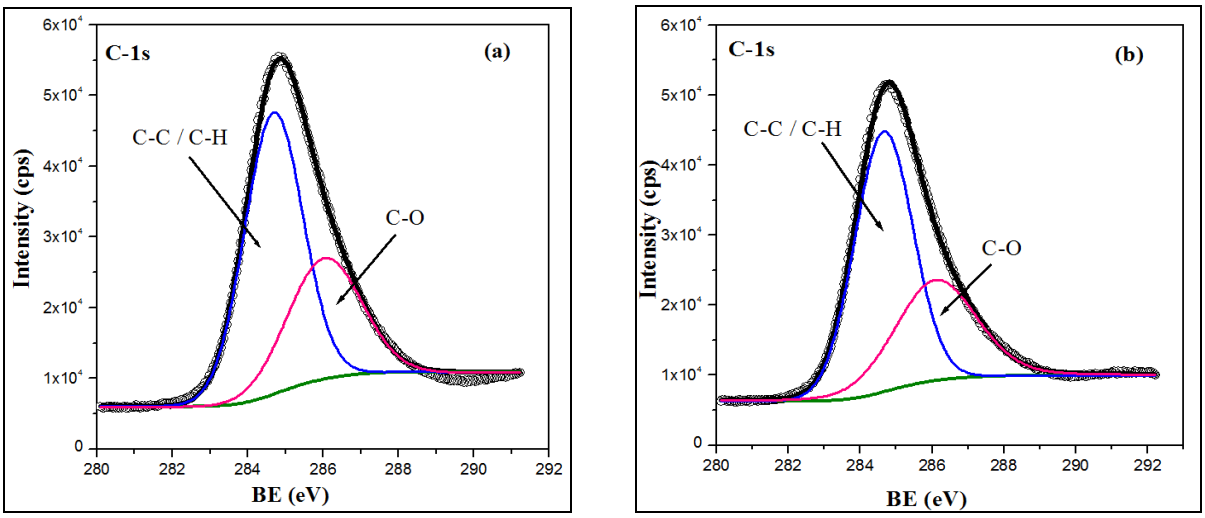

Fig. 5 High resolution C-1s photoelectron spectra obtained from skin layers of (a) Ps UF and (b) Ps-nRGO UF-2 (line with bullets: experimental data; solid line: curve fit of the experimental data).

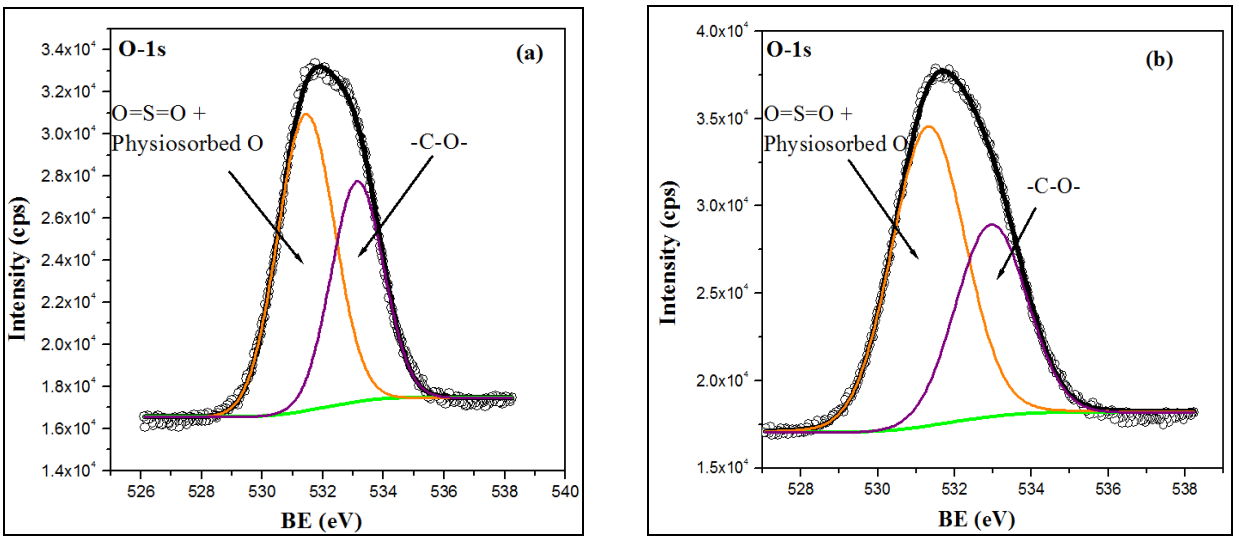

Fig. 6 High resolution O-1s photoelectron spectra obtained from skin layers of (a) Ps UF and (b) Ps-nRGO UF-2 (line with bullets: experimental data; solid line: curve fit of the experimental data).

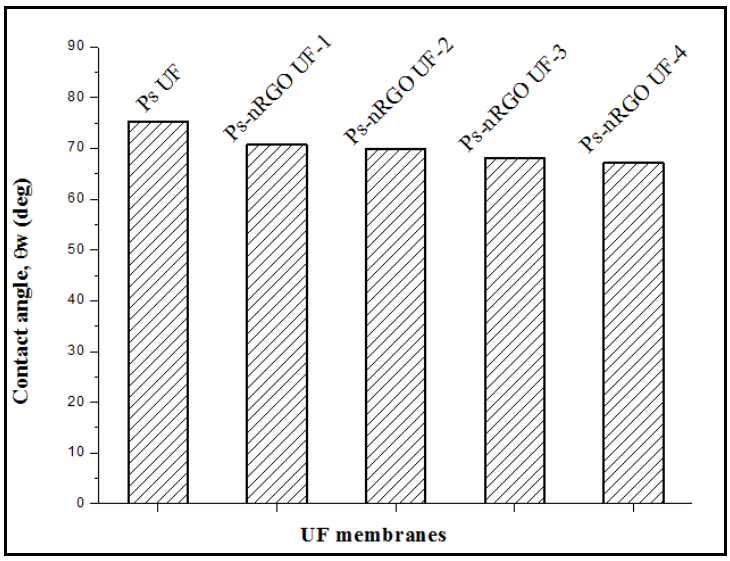

Fig. 7 Variation in contact angles (water) of Ps UF and Ps-nRGO composite UF membranes.

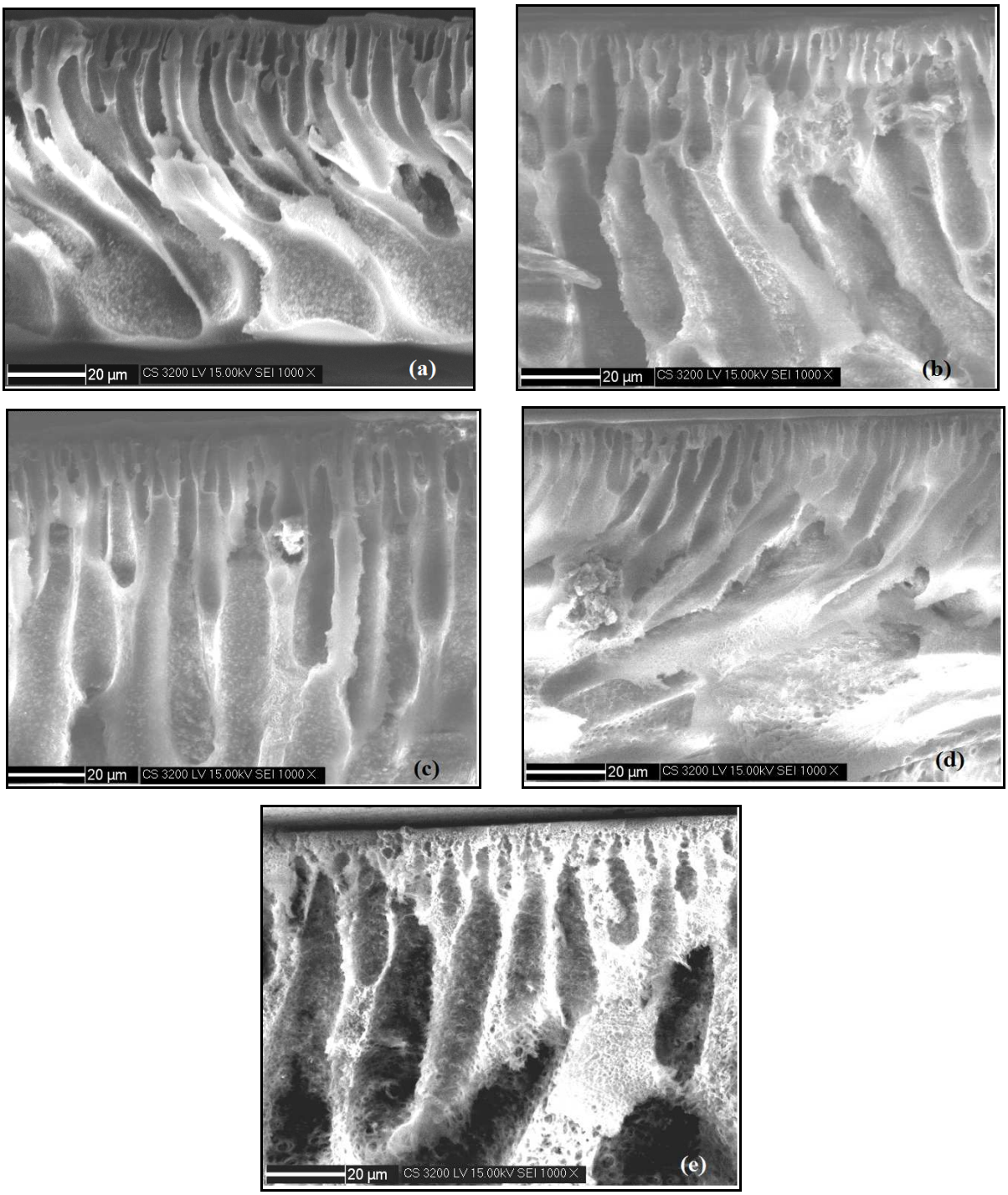

Fig. 8 Cross-sectional SEM images of membranes: (a) Ps UF, (b) Ps-nRGO UF-1, (c) Ps-nRGO UF-2, (d) Ps-nRGO UF-3 and (e) Ps-nRGO UF-4.

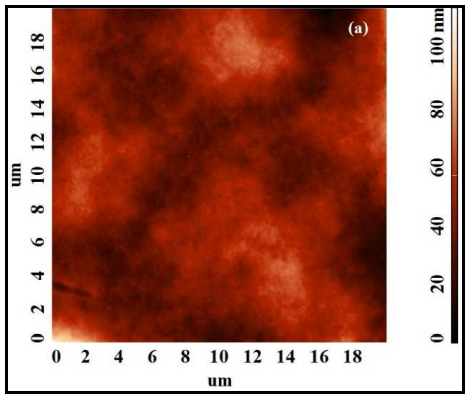
(a)
um
um
nm

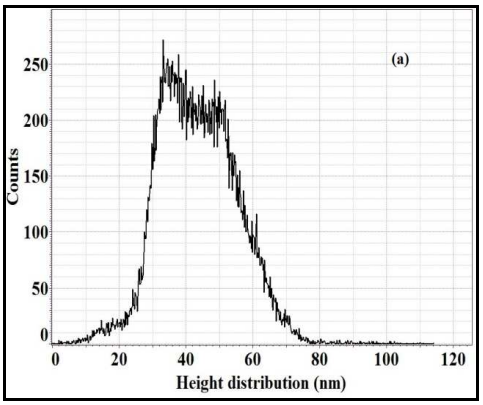
(a)
Counts
Height distribution (nm)

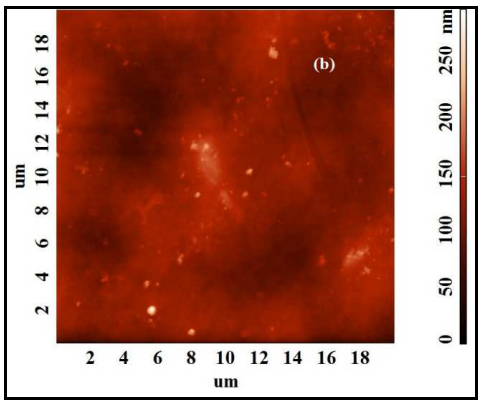
(b)
um
um
nm

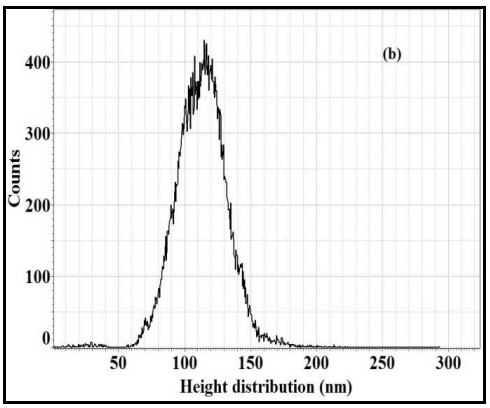
(b)
Counts
Height distribution (nm)

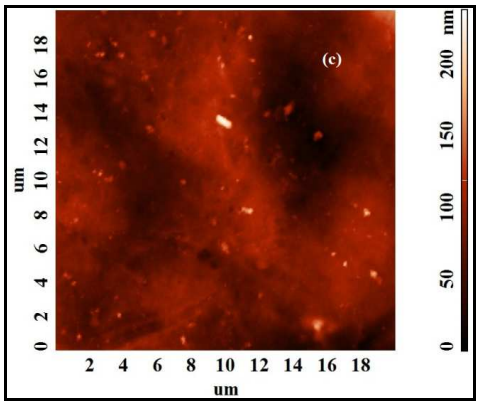
(c)
um
um
nm

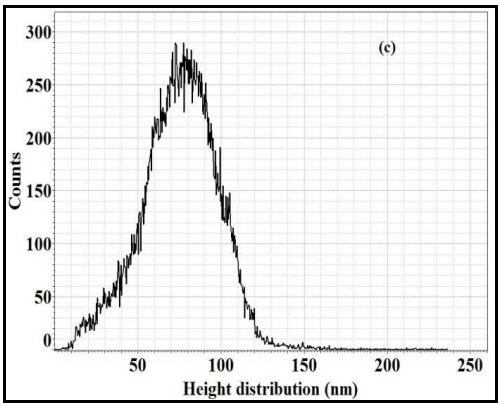
(c)
Counts
Height distribution (nm)

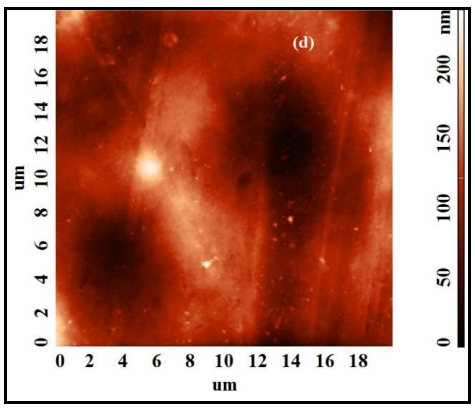
(d)
um
um
nm

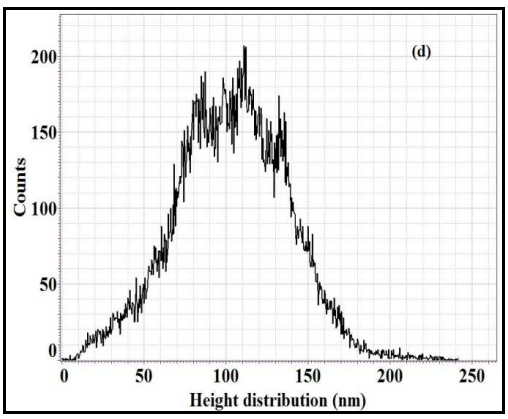
(d)
Counts
Height distribution (nm)

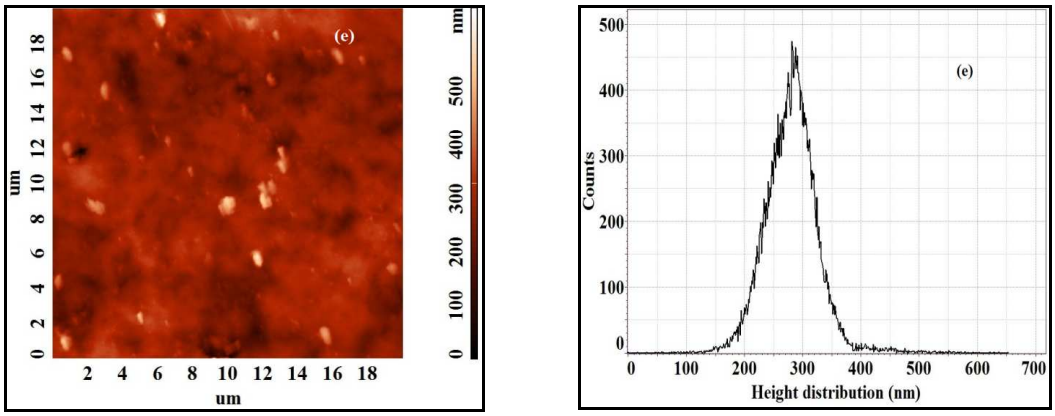

Fig. 9 2D AFM images and height histograms of (a) Ps UF, (b) Ps-nRGO UF-1, (c) Ps-nRGO UF-2, (d) Ps-nRGO UF-3 and (e) Ps-nRGO UF-4.

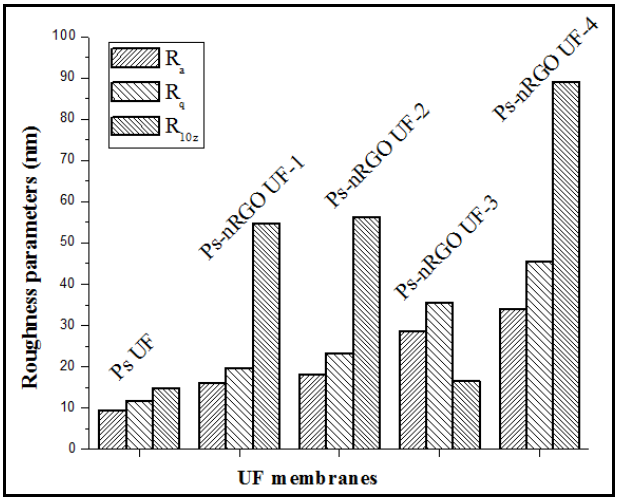

Fig. 10 Surface roughness parameters of Ps UF and Ps-nRGO composite UF membranes.

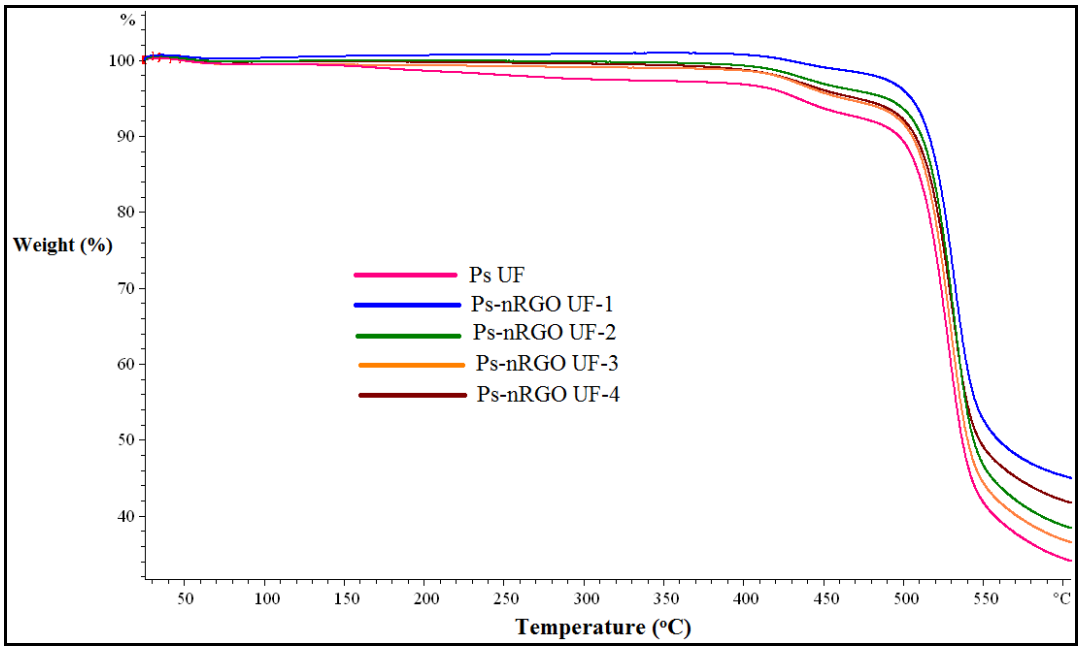

Fig. 11 TGA Thermograms of pure Ps UF and Ps-nRGO composite UF membranes.

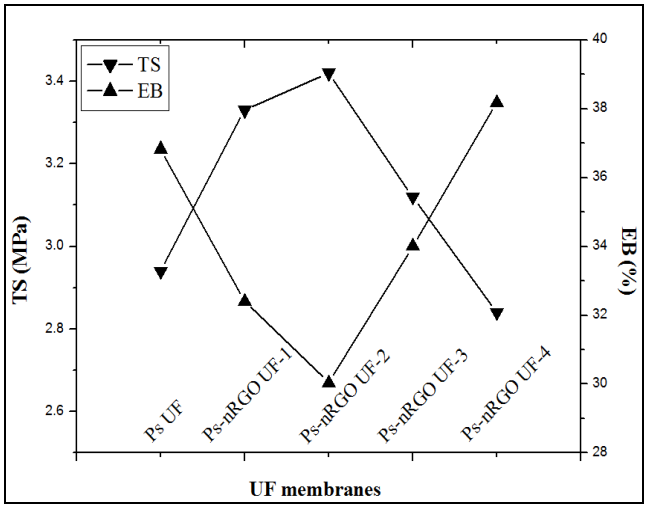

Fig. 12 Variation in mechanical features for Ps UF and Ps-nRGO composite UF membranes.

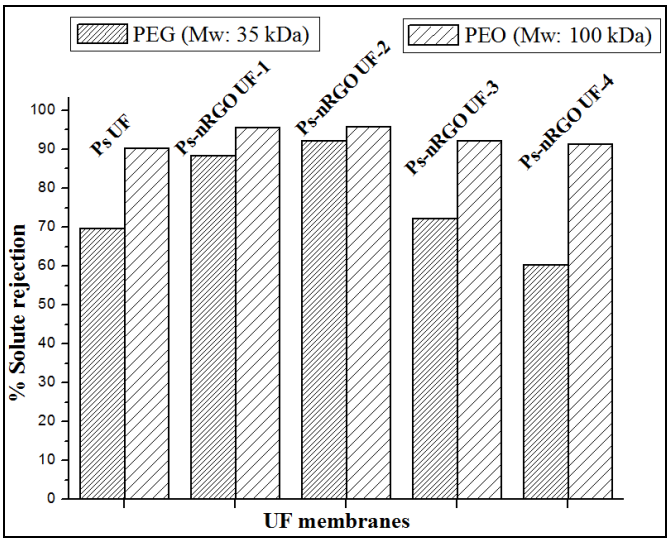

Fig. 13 Solute rejection behavior of Ps UF and Ps-nRGO nanocomposite UF membranes.

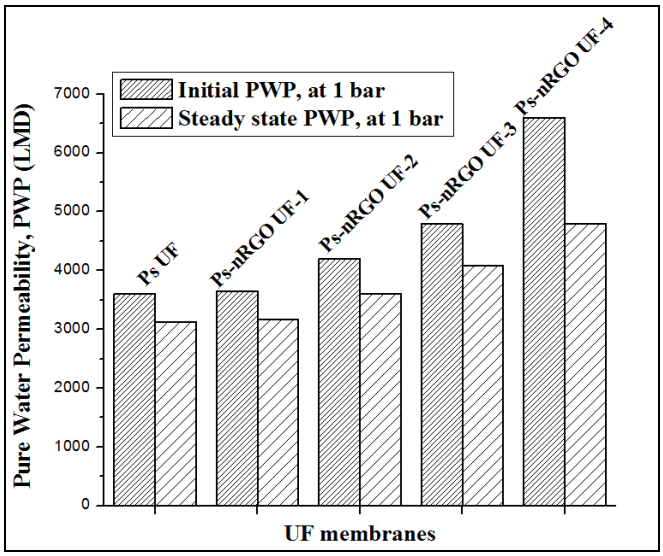

Fig. 14 PWP behavior of Ps UF and Ps-nRGO nanocomposite UF membranes.

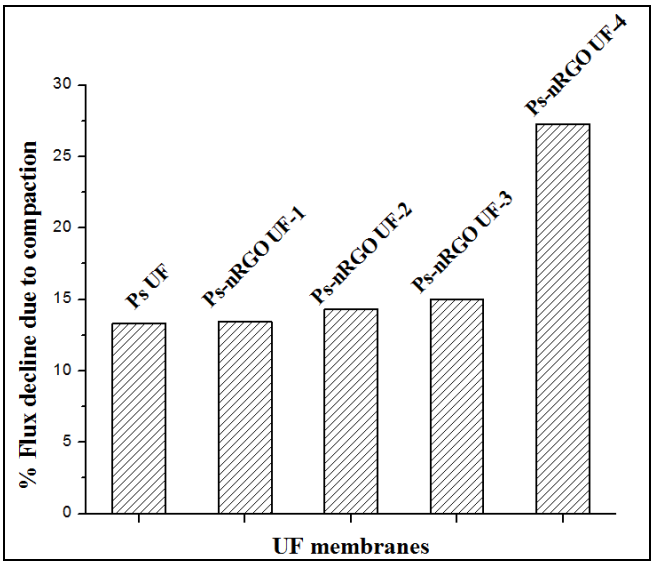

Fig. 15 Variation in flux due to compaction in the matrices of Ps UF and Ps-nRGO composite UF membranes.

Table 1 Curve fitting summary of different XPS peaks for nRGO.

Material	C-1s			O-1s		
	BE (eV)	FWHM (eV)	Peak area (%)	BE (eV)	FWHM (eV)	Peak area (%)
nRGO	284.6	1.55	28.16	530.1	1.39	3.37
	285.8	1.54	16.64	533.2	3.62	96.63
	286.5	2.58	39.16			
	289.2	4.39	16.04			

Table 2 Curve fitting summary of different XPS peaks for Ps UF and Ps-nRGO UF-2.

Material	C-1s			O-1s		
	BE (eV)	FWHM (eV)	Peak area (%)	BE (eV)	FWHM (eV)	Peak area (%)
Ps UF	284.7	1.93	66.67	531.3	2.20	59.47
	286.1	2.59	33.33	533.0	2.02	40.53
Ps-nRGO UF-2	284.7	1.91	63.49	531.3	2.25	62.45
	286.1	2.66	36.51	533.0	2.18	37.55

Table 3 Thermal features and tensile properties of Ps UF and Ps-nRGO composite UF membranes.

Membrane Code	Thermal features		Mechanical features	
	T_d (^oC)	Mass loss (%)	TS (MPa)	EB (%)
Ps UF	507.8	57.61	2.94 ± 0.16	36.83
Ps-nRGO UF-1	513.5	51.56	3.33 ± 0.11	32.41
Ps-nRGO UF-2	512.9	53.61	3.42 ± 0.07	30.04
Ps-nRGO UF-3	509.7	54.01	3.12 ± 0.19	34.01
Ps-nRGO UF-4	510.4	52.55	2.84 ± 0.24	38.18